ACS OMEGA

http://pubs.acs.org/journal/acsodf

Article

Process Optimization of Para-xylene Crystallization Separation Process via Morphology Approach, Multi-dimensional Population Balance Equation, and Equation-Oriented Models

Zhenxing Cai, Hui Zhao, Pingxin Li, Xiaobo Chen, and Chaohe Yang*

Cite This: *ACS Omega* 2023, 8, 12899−12910

Read Online

ACCESS | Metrics & More | Article Recommendations | Supporting Information

ABSTRACT: An activity coefficient-based model was proposed to predict pertinent saturated concentrations in organic solid−liquid equilibrium, and the binary parameters of xylene mixtures were experimentally obtained. Also, a novel monocular 3D reconstruction technique was developed to measure crystal size and applied to derive the kinetics of nucleation and growth of para-xylene crystals. Subsequently, a multi-dimensional population balance equation was used to predict the particle size distribution in the crystallizer and an algorithm was designed to simulate and optimize the economic benefit of the crystallization separation process. Consequently, it became possible to predict the optimal coolant flowrate and inlet temperature, as well as the feed flowrate for a crystallization process with given operating conditions and device parameters.

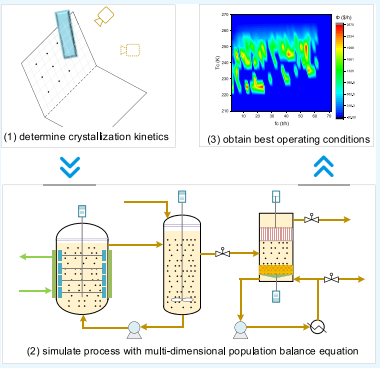

1. INTRODUCTION

Para-xylene (PX) is the precursor chemical for the production of dimethyl terephthalate and terephthalic acid, which are used in the manufacture of polyethylene terephthalate bottles, fibers, and films.[1] PX is primarily purified from xylene mixtures, a petroleum product, that contains ortho-xylene (OX), meta-xylene (MX), PX, and ethyl-benzene (EB). PX, OX, and MX have similar boiling points but different freezing points and molecular structures. Thus, the distillation separation approach is not a suitable means of purification. Instead, adsorption was the best option before the 2000s, but with the development of isomerization catalysts, the fraction of PX in xylene mixtures from isomerization reactors has been greatly enhanced, typically yielding more than 65 wt %.[2] Alternatively, the crystallization method does not introduce an adsorbent, has fewer units, and can be operated continuously. Such advantages have resulted in it being widely adopted by new built factories. Figure 1 is a suspension crystallization separation process flow diagram from industry,[3] which is composed of two loops, one for crystallization and the other for separation. The first contains a crystallizer and a growth vessel. PX particles crystallize on the wall of the crystallizer before they are scraped away into solution, which is circulated into the growth vessel, where they undergo crystal growth. After the particles are mature (i.e., they are deemed large enough), they proceed into the separation loop where the products are obtained by driving the solution through a wash column, aided by a piston.

The functional steps of the wash column as illustrated in Figure 2 are the following: (1) filling step (the piston moves up, drawing in the slurry from the growth vessel, and residue above the piston is simultaneously ejected); (2) compression step (the piston's downward movement forces the slurry's mother liquor through the filter screen, so only the PX particles, with few impurities, are left below it); (3) washing step (the piston continues to move downward, forcing the remnants of the high-purity PX liquid to pass through the original cake and the newly formed cake); and (4) scraping step (the blades rotate and scrape the cake, reducing it to particles again, which are then transferred to the melting unit, from which the final PX product is obtained).

The morphology and size of the particles have a significant impact on the product yield. Those that are small can pass through the filter screen easily and may thus dissolve into the liquid phase again during the washing step. Generally, PX particles have distinct morphologies, structural strengths, and sizes in different growth environments. For example, the particles grow more quickly at higher supersaturation but also become thinner and more fragile. As illustrated in Figure 3, four particles were formed in four different levels of supersaturation, and the first two kinds listed were non-fragile and the most desirable. Aggregation occurred in the last one,

Received: January 4, 2023
Accepted: March 17, 2023
Published: March 31, 2023

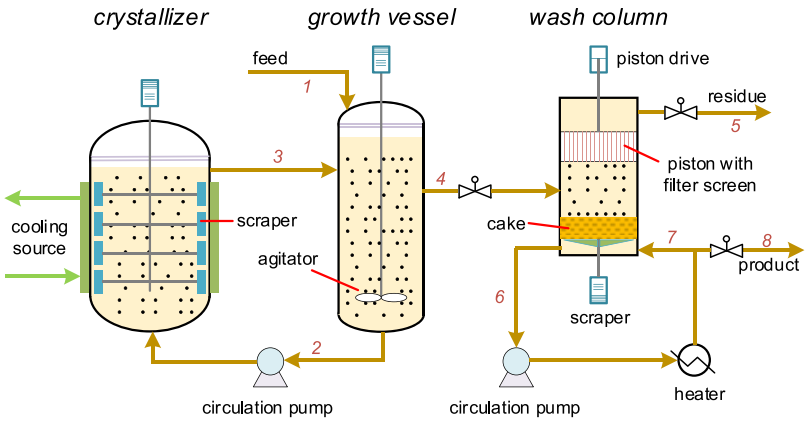

Figure 1. PX suspension crystallization separation process[3] (adapted with permission from ref 3. Copyright 2019 Cambridge University Press)

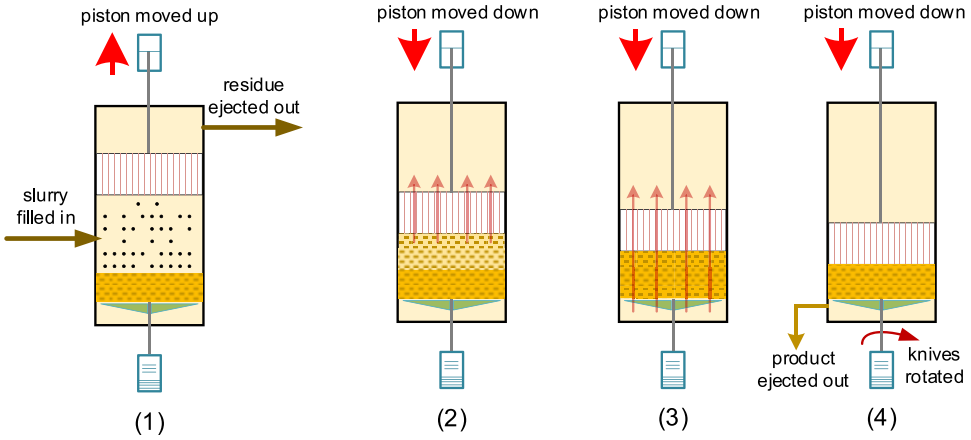

Figure 2. Functional steps of the wash column[3] (adapted with permission from ref 3. Copyright 2019 Cambridge University Press)

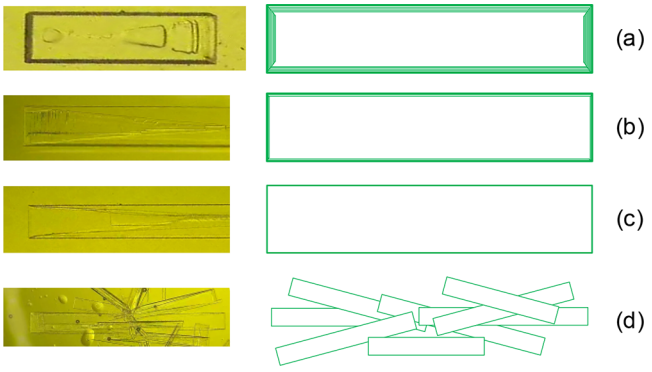

Figure 3. Different morphologies of PX particles growing up at solutions of (a) low saturated, (b) medium saturated, (c) high saturated, and (d) super-high saturated.

resulting in a vague conglomerate composed of loosely bonded small particles, which can disassemble into small fragments during subsequent operations. Naturally, this morphology is far from ideal in the product.

The solubility data, as well as the nucleation and growth kinetics of PX crystallization, should be determined to control and optimize the separation process. However, there are only a few instances of this reported in literature. In one of these investigations, Jakob et al.[4] determined the binary solid−liquid equilibrium data of xylene isomers using the synthetic method, but the ternary solubility experiment was not carried out and no theory was proposed to predict PX solubility in ternary mixtures. Elsewhere, De Goede et al.[5] measured the binary solid−liquid equilibrium data of PX/OX and PX/MX using the DSC approach, but the experimental PX fraction range was limited to above 70% of the weight. De Goede and Van Rosmalen[6] also measured the growth rate of PX particles separately using a morphological approach. However, although the PX particle is a rectangular plate and the growth rates are anisotropic, they still measured the growth rate in the length direction and assumed that the growth rate was a function of temperature, which ignores the effect of the fraction. Meanwhile, Mohameed et al.[7] predicted the change in weight of PX particles by measuring the solution's concentration in real time but did not consider the anisotropy of growth rate caused by particle shape. Moreover, Patience et al.[1] predicted the quantity of PX particles by measuring the slurry transmittance and estimated the kinetic parameters of the PX crystallization process.

The PX crystallization separation technique is a single-compound-precipitation process. All the compounds in the mixture are organic, meaning electrolyte theory[8] is not applicable. Polynomial models (e.g., Apelblat equation,[9] λH equation[10]) are other approaches for predicting solubility in the solid−liquid equilibrium, but the parameters of these models are fitted from experiments and only applicable in cases with similar experimental conditions. To avoid the shortage of reported work addressing this, new experiments, models, and approaches should be developed to enhance the accuracy of predictions.

https://doi.org/10.1021/acsomega.3c00069
ACS Omega 2023, 8, 12899−12910

Table 1. Solubility Data for Binary Mixtures of PX(1) + OX(2), PX(1) + MX(2), and OX(1) + MX(2)[a]

x_1	T/K	x_1	T/K	x_1	T/K
PX(1) + OX(2)		0.917	283.0	0.794	278.3
0.250	237.3	0.951	283.8	0.845	280.8
0.302	244.5	PX(1) + MX(2)		0.900	282.8
0.372	250.4	0.179	229.1	0.952	284.8
0.405	254.2	0.210	233.1	OX(1) + MX(2)	
0.420	255.4	0.239	237.9	0.355	212.4
0.435	257.0	0.265	241.0	0.402	216.1
0.483	260.6	0.292	245.2	0.446	219.7
0.515	262.9	0.341	249.4	0.504	223.7
0.556	264.6	0.374	252.2	0.550	227.0
0.577	265.7	0.406	254.7	0.601	230.1
0.634	268.6	0.448	258.1	0.654	232.6
0.672	271.2	0.515	263.5	0.701	235.0
0.712	274.0	0.543	264.1	0.747	236.9
0.756	275.3	0.585	267.7	0.798	240.0
0.778	276.5	0.650	270.5	0.844	241.6
0.833	279.3	0.695	272.9	0.892	243.3
0.884	281.3	0.757	276.2	0.951	245.4

[a]Standard uncertainties are $u(T) = 0.1$ K, $u(p) = 0.05$ kPa, and $u(x) = u(y) = 0.001$.

In this paper, the classical solid−liquid equilibrium theory was combined with the activity coefficient model. By correlating the binary parameters of the UNIQUAC method from experimental data, the saturation concentration of PX in any multicomponent mixture can be predicted by the UNIQUAC model. After that, the growth of PX crystals was observed and measured in an environment with fixed temperatures and concentrations, from which the growth rate can be determined as a function of supersaturation. The nucleation rate was also identified as a function of supersaturation and controlled by the flow rate and inlet temperature of the coolant. Based on the previously developed crystallization kinetic models, the particle size distribution in the crystallizer was predicted by a three-dimensional population balance equation,[11] from which the optimal yield can be derived by adjusting the control variables.

2. KINETICS MODELS AND EXPERIMENTAL DETERMINATION

2.1. Saturation Concentration of PX in Xylene Mixtures. A DSC experiment for determining the solubility of binary xylene mixtures was conducted, the experimental methods have been reported in our previously published work,[12] and the measured results are presented in Table 1 and compared with literature values[4] in Figure 4.

For organic systems without ionization, when the solid and liquid phases reach an equilibrium status, the concentration x_i of precipitated compound i in liquid is a function of temperature T and activity coefficient γ_i, as given in eq 1:

$$\ln(x_i) = \frac{\Delta H_m}{R}\left(\frac{1}{T_m} - \frac{1}{T}\right) - \ln(\gamma_i) \quad (1)$$

where ΔH_m is the molar melting enthalpy at normal melting point T_m and R is the universal gas constant. The activity coefficient γ_i can be calculated by applying activity coefficient models, of which UNIQUAC, one of the most widely known, is provided in eqs 2−6:

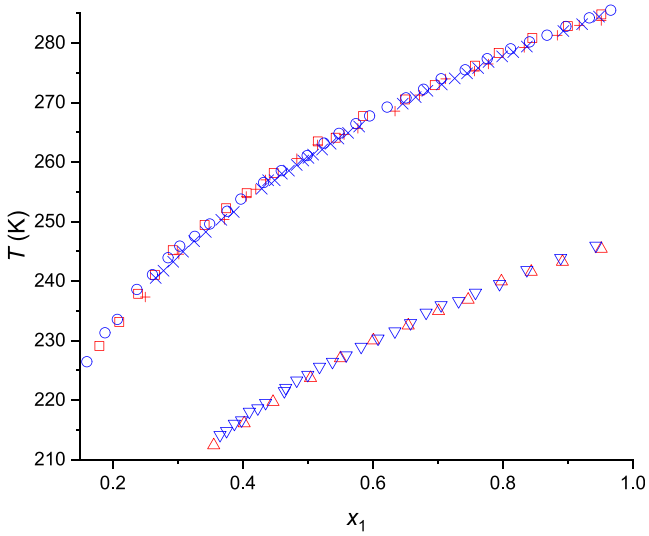

Figure 4. Solubility data of binary xylene mixtures: plus symbol, PX(1) + OX(2) measured; multiplication symbol, PX(1) + OX(2) from Jakob et al.;[4] square, PX(1) + MX(2) measured; circle, PX(1) + MX(2) from Jakob et al.;[4] triangle, OX(1) + MX(2) measured; inverted triangle, OX(1) + MX(2) from Jakob et al.[4]

$$\ln(\gamma_i) = \ln\frac{\varphi_i}{x_i} + Z\cdot q_i\cdot\ln\left(\frac{\theta_i}{\varphi_i}\right)/2 + l_i - \frac{\varphi_i}{x_i}\sum_k x_k l_k - q_i\ln\left(\sum_k \theta_k\tau_{ki}\right) + q_i - q_i\sum_k \frac{\theta_k\tau_{ik}}{\sum_j \theta_j\tau_{jk}} \quad (2)$$

$$\varphi_i = \frac{r_i x_i}{\sum_k r_k x_k} \quad (3)$$

$$\theta_i = \frac{q_i x_i}{\sum_k q_k x_k} \quad (4)$$

$$l_i = \frac{Z}{2}(r_i - q_i) - (r_i - 1) \quad (5)$$

https://doi.org/10.1021/acsomega.3c00069
ACS Omega 2023, 8, 12899−12910

$$\tau_{ij} = \exp\left(\frac{b_{ij}}{RT}\right) \tag{6}$$

where r and q are the van der Waals volume and area parameters, respectively; all xylene isomers have the same r and q parameters and take values of 7.066×10^{-5} m^3/mol and 8.84×10^5 m^2/mol, respectively. Z is the lattice coordination number, which is 6 for xylene isomers. b_{ij} is the binary parameter between compounds i and j, and independent on temperature and composition. The activity coefficient γ_i is a function of concentration x_i and temperature T. The binary parameters b_{ij} are used to calculate the residual and combinatorial parts of the activity coefficient, which were fitted from the solubility data presented in Table 1, and their results are collated in Table 2. The binary parameters are temperature independent and can be applied on ordinary conditions.

Table 2. Fitted UNIQUAC Binary Parameters b_{ij} of Xylene Mixtures and Corresponding Root Mean Square Errors (RMSD)

	b_{12}	b_{21}	RMSD
PX/OX	1171.747	−1477.523	0.0074
PX/MX	983.770	−1242.609	0.0085
OX/MX	885.881	−372.688	0.0040

By replacing the term $\ln(\gamma_i)$ of eq 1 with eq 2, the concentration x_i (i.e., the saturation concentration) becomes a function of temperature, and vice versa. This is a very common thermodynamic approach to predict solubility and has been adopted in a large quantity of published research. For example, Gmehling et al.[13] predicted the solubility of naphthalene in alcohol−water mixtures and anthracene in acetone−ethanol mixtures using UNIFAC, and the results correlated well with experiments. Also, Boudouh et al.[14] predicted the solid−liquid equilibrium diagrams of ternary mixtures with UNIFAC, UNIFAC−Lyngby, and UNIFAC−Dortmund equations, and in each case, the models were applicable for specific mixtures. In addition, Valavi et al.[15] used NRTL-SAC and UNIFAC to predict the solubility of pharmaceutical compounds in organic solvents.

In this work, the re-arranged equation from eqs 1 and 2 is nonlinear and should be solved by iteration and implemented by the fsolve method from MATLAB. The solubility of PX in ternary mixtures was also measured via the methods presented in our previous work,[12] and the mole fraction ratio between OX and MX was fixed at 0.331: 1; the obtained results are tabulated in Table 3. Besides, the prediction of ternary mixtures is compared with experiments in Table 3 and Figure 5, which verified the reliability of the proposed models and fitted binary parameters.

2.2. Nucleation Kinetics. The classical nucleation theory expresses the nucleation rate R_n via the Gibbs−Thompson equation, as follows:[16]

$$R_n = \exp\left(\frac{-\Delta G_{crit}}{k_B T}\right) \tag{7}$$

where k_B, T, and ΔG_{crit} represent the Boltzmann constant, temperature, and critical free energy change, respectively. During the nucleation process, as presented in Figure 6, a crystal's continuous growth can only occur when its embryo is larger than a critical size, while any which are smaller are thermodynamically inclined to dissolve.[17] Gibbs suggested that the free energy difference between the monomers in solution and formed nuclei is the activation free energy, where ΔG_{crit} corresponds to the critical size.[18]

Table 3. Measured (x_1^e) and Predicted (x_1^p) Solubility of PX (1) in a Ternary Mixture of Xylenes, with a Fraction Ratio between OX and MX of 0.311[a]

T/K	x_1^e	x_1^p	T/K	x_1^e	x_1^p
239.6	0.254	0.258	269.8	0.643	0.639
244.0	0.297	0.297	272.5	0.696	0.705
250.1	0.363	0.365	275.3	0.749	0.744
255.4	0.420	0.417	277.7	0.801	0.802
259.7	0.483	0.482	280.0	0.851	0.845
263.6	0.541	0.537	282.3	0.900	0.906
266.3	0.590	0.582	284.3	0.950	0.943

[a]Standard uncertainties are $u(T) = 0.1$ K, $u(p) = 0.05$ kPa, and $u(x) = u(y) = 0.001$.

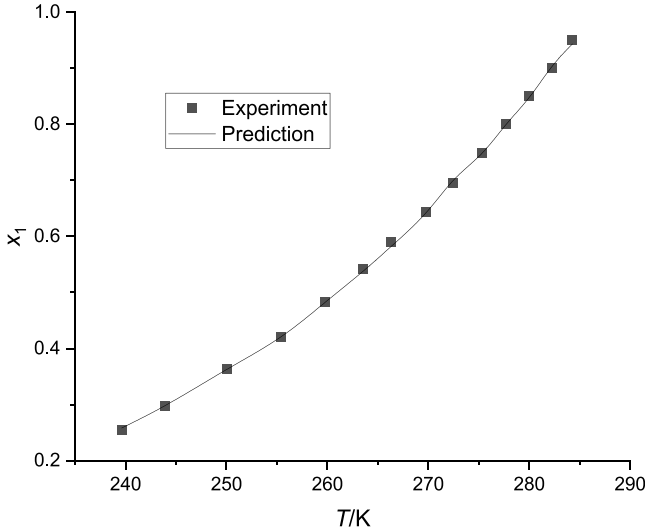

Figure 5. Fit of solubility of PX in xylene mixtures as predicted by UNIQUAC and from experimental measurements, with a fraction ratio between OX and MX of 0.311.

According to classical nucleation theory, the total free energy required to form a spherical crystallite with radius r can be stated as below:[19]

$$\Delta G = \Delta\mu\left(\frac{4}{3}\pi r^3\right)\rho_s + 4\pi r^2\gamma \tag{8}$$

where $\Delta\mu$ is the chemical potential difference between solid and liquid, ρ_s is the number density of the solid, and γ is the solid−liquid interfacial free energy density. When the radius r reaches the critical size $-2\gamma/(\rho_s\Delta\mu)$, ΔG_{crit} becomes $16\pi\gamma^3/[3(\rho_s\Delta\mu)^2]$ transforming eq 8:

$$R_n = \exp\left(-\frac{16\pi\gamma^3}{3k_B T(\rho_s\Delta\mu)^2}\right) \tag{9}$$

Because the complexity of eq 9 is borne out by the fact that many terms cannot be measured or calculated, Hounslow et al.[20] proposed a simplified nucleation rate model as a function of supersaturation, which is adopted and expanded upon in this work:

https://doi.org/10.1021/acsomega.3c00069
ACS Omega 2023, 8, 12899−12910

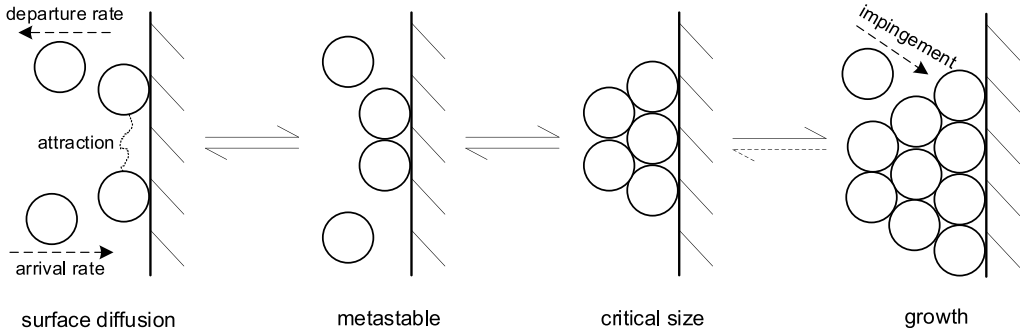

Figure 6. Process of nucleation of crystals on a surface.

$$R_n(T, c) = k_n^1\left(\frac{c - c^*}{c^*}\right)^{k_n^2} \tag{10}$$

where k_n^1 and k_n^2 are two constant coefficients for a specific mixture, c is the solution concentration of the compound to be precipitated, and c^* is the saturation concentration, which is a function of temperature T as defined in a previous section. As an exemplar, measurements of the heterogeneous rate at different temperatures and concentrations were taken in a beaker immersed within coolant. The solution was mixed well by a stirrer at low rotating speed, and the number of crystals was counted after stirring stopped. By adjusting the solution concentration within the beaker and the coolant's temperature, the number of crystallites on the interior surface and in solution was recognized by OpenCV and recorded against time. The saturation concentration was calculated according to temperature and the equations as detailed in Section 2.1, up to and including the point of supersaturation. The nucleation rates at different supersaturations are presented in Figure 7,

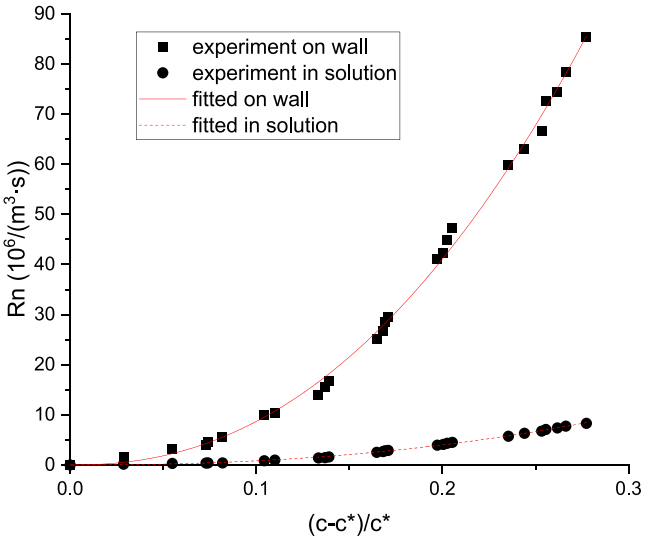

Figure 7. Nucleation rates at different levels of supersaturation.

where the parameters k_n^1 and k_n^2 on the wall were fitted to be 1.516×10^9 and 2.242, respectively, with a standard deviation of 0.085; the k_n^1 and k_n^2 in the solution were fitted to be 1.571×10^8 and 2.280, respectively, with a standard deviation of 0.043.

The crystal nuclei that formed on the inside wall of the crystallizer were mechanically removed into solution by rotating scrapers. The temperature of the coolant increased from the bottom of the vessel up, while that of the crystallizer wall was assumed to be the average temperature of the coolant outside and solution inside; i.e., the nucleation rates differed along the vertical direction. The total nucleation rate R_n^c in the crystallizer is given below:

$$R_n^c(t) = \int_0^{h_1} 2\pi r_1 R_n^{\text{wall}}\left(\frac{T_c(t, z) + T_s(t)}{2}, c\right)dz + R_n^{\text{solution}} \tag{11}$$

2.3. Crystal Growth Kinetics. The typical PX crystal is a rectangular plate (as shown in Figure 3), and its growth kinetics are described by the rates at which its width, length, and thickness increase. However, most research portrays the 3D representation of a PX crystal as a sphere with equivalent radius, which is measured or predicted by slurry transmittance,[1] solution concentration change,[7] or only on length direction.[6] Crystal 3D reconstruction has been carried out by few researchers,[21] but two or more cameras were needed and fixed around the crystal (see Figure 8a); the lens should not be

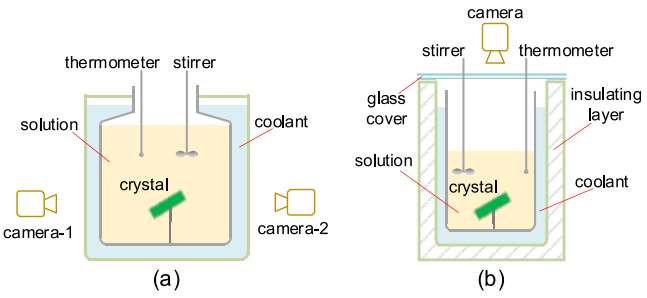

Figure 8. Experimental equipment for 3D reconstruction: (a) conventional for moderate temperatures; (b) proposed setup for deep cold conditions as detailed in this work.

frosted or immersed within coolant, which is only practical for experimental conditions with moderate temperatures. However, the crystallization separation operating temperature of xylene mixtures may be as low as 200 K, necessitating the apparatus to be fixed in a deep groove with one viewing port, and the camera can only be installed above the groove (see Figure 8b), due to which a conventional approach was not possible. During the deep cold experiment, the glass cover and camera were purged by nitrogen; thus, the glass cover and camera were kept at a low temperature and in a dry environment, and the frosting phenomenon can be prevented. The solution was mixed well by a stirrer at low rotating speed; the crystal can remain fixed and be observed continuously.

To deal with the shortage of former studies, a crystal 3D reconstruction equipment with a single camera was proposed.

https://doi.org/10.1021/acsomega.3c00069
ACS Omega 2023, 8, 12899−12910

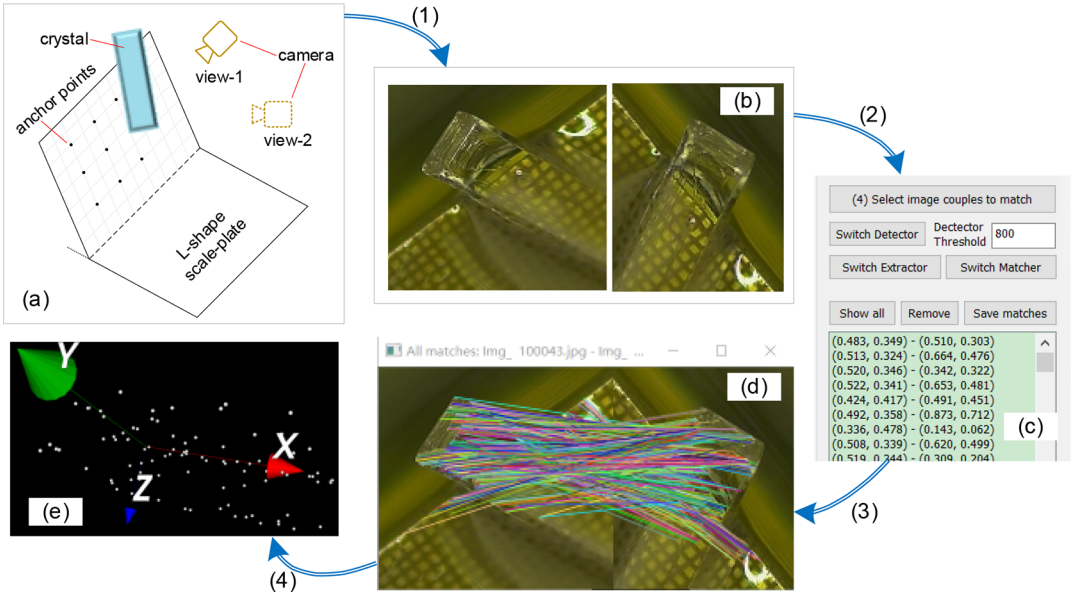

Figure 9. Monocular 3D reconstruction process of crystals: (1) camera calibration; (2) feature detection; (3) feature matching; and (4) spatial coordinate prediction. The elements during 3D reconstruction: (a) the L-shape scale plate and camera views; (b) the captured images of crystal; (c) the developed software for feature detecting and matching; (d) matched features; and (e) the predicted spatial coordinates.

As presented in Figure 9a, an L-shape card was made from a scale plate upon which the crystal was placed. Even though the camera location was fixed above the equipment (see Figure 8b), by rotating the scale plate or changing the folding angle, two views on one crystal from different perspectives can be shot (see Figure 9b). Then, the combination of the two views can be used for 3D reconstruction.

The monocular 3D reconstruction technique mainly consists of the following procedures:

(1) Camera calibration

The projection of the image captured by the camera is typically interpreted by the pinhole concept, whereby the spatial coordinate (p_x^w, p_y^w, p_z^w) and its image projection (p_x^m, p_y^m) are given by[22]

$$\begin{bmatrix} p_x^m \\ \rho(p_y^m) \\ 1 \end{bmatrix} = \begin{bmatrix} f_x & -f_x \cot\theta & p_{x0}^m & 0 \\ 0 & f_y/\sin\theta & p_{y0}^m & 0 \\ 0 & 0 & 1 & 0 \end{bmatrix} \begin{bmatrix} \boldsymbol{R}^m & \boldsymbol{T}^m \\ 0 & 1 \end{bmatrix} \begin{bmatrix} p_x^w \\ p_y^w \\ p_z^w \\ 1 \end{bmatrix} \quad (12)$$

where ρ is an arbitrary scale factor; p_{x0}^m, p_{y0}^m, θ, f_x, and f_y are camera intrinsic parameters; and $\boldsymbol{R}^m$ and $\boldsymbol{T}^m$ are rotation and translation matrices. As noted in Figure 10, for four spatial points (a_w, b_w, c_w, and d_w) in the same plane and separated by an identical distance Δd, the projected points (a_m, b_m, c_m, and d_m) on the image should also be separated by an identical distance Δl, which can be calculated using eq 12. However, due to camera distortion, Δl_1, Δl_2, Δl_3, and Δl_4 are different, i.e., the captured image deviates from reality to some extent. The relation between the distorted coordinate (p_x^m, p_y^m) and the unobservable, distortion-free image point (p_x^{mc}, p_y^{mc}) can be described using eq 13.[23]

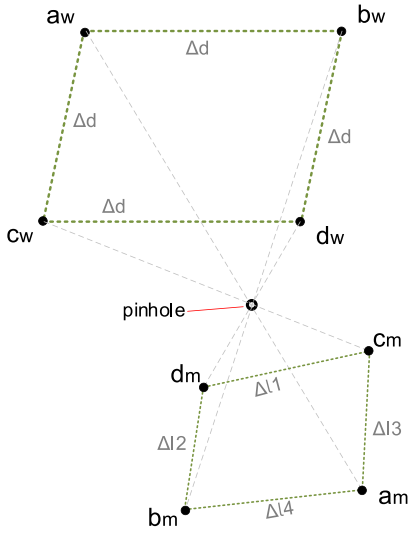

Figure 10. The pinhole theory for camera projection

$$\begin{bmatrix} p_x^m \\ p_y^m \end{bmatrix} = \begin{bmatrix} p_x^{mc} \\ p_y^{mc} \end{bmatrix} + \begin{bmatrix} \delta_x(p_x^{mc}, p_y^{mc}) \\ \delta_y(p_x^{mc}, p_y^{mc}) \end{bmatrix} \quad (13)$$

where δ_x and δ_y are distortion functions. If the spatial coordinates (a_w, b_w, c_w, and d_w), spatial distance (Δl), and their corresponding coordinates (a_m, b_m, c_m, and d_m) and distances (Δl_1, Δl_2, Δl_3, and Δl_4) on the image are known, the unknown parameters in eqs 12 and 13 can be obtained. Overall, this process describes the camera calibration. In practice, four coordinates are not enough, nine or more are required (the more the better). In Figure 9a, nine anchor points were selected from the L-shape scale plate. The L-shape scale plate was made manually from a general scale plate for microscope and played a role of chessboard during camera calibration. The anchor points had uniform distances between pairs so as to form a grid on a single plane, and the top left one

https://doi.org/10.1021/acsomega.3c00069
ACS Omega 2023, 8, 12899−12910

was assumed to be the original point. As a result, the coordinates (p_x^w, p_y^w, p_z^w) of the anchor points can be identified. The corresponding coordinates (p_x^m, p_y^m) on the image were detected by the HoughLinesP method from OpenCV. Subsequently, the image was calibrated by the calibrateCamera, initUndistortRectifyMap, and remap tools, which are part of the OpenCV suite. Upon such treatment, the coordinates of any pixel on the image were no longer distorted, which can then be used for the subsequent steps.

(2) Feature detection and matching

"Local feature" refers to a distinct section found in an image, such as a point, edge, or patch, meaning that two photos taken, ostensibly of the same object, from different perspectives should share a significant proportion of local features. Feature detection is an approach to compute the abstraction of image information relating to these local features. To this end, many algorithms have been proposed and implemented in OpenCV, such as the algorithms SIFT, SURF, FAST, BRIEF, and ORB. The detected features also need to be matched, and OpenCV provides FlannBasedMatcher and BFMatcher to implement these requirements. For this work, an easy-to-use program was developed using C++ and OpenCV (see Figure 9c), and since it is difficult to select the best feature detection or matching algorithm automatically, the configuration is to be adjusted manually. The matched features were connected by lines, as in Figure 9d.

(3) Spatial coordinate prediction

As shown in Figure 11, assuming the camera was calibrated and a known point p_1^m on image 1 was determined, according to

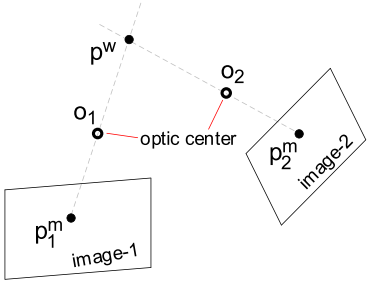

Figure 11. Spatial coordinate prediction from two matched feature points.

eq 12, the spatial point p^w of the captured object must be on the line $p_1^m o_1$. Then, assuming p_2^m is the matched feature point of p_1^m on another image 2, p^w must also be on the line of $p_2^m o_2$. Consequently, the spatial coordinate p^w can be derived from the intersection of two lines $p_1^m o_1$ and $p_2^m o_2$. However, due to the small errors between matched features or equipment defect, these two lines may never intersect and instead have a minimum separation distance. If the minimum distance is less than a given tolerance (for example 0.05 mm), the two lines are considered to fully intersect and the middle point of the minimum line segment is assumed to be the coordinate of spatial point p^w. All the predicted spatial points were rendered using the program VTK, as illustrated in Figure 9e. This resulted in confirmation of the crystal's size and dimensions.

By carrying out the above measurements against time, the three-dimensional size change of PX crystal in the three axes were recorded. The growth rate R_g can be assumed to be a function of supersaturation, as per eq 14. Results are listed in Figure 12, and the parameters k_g^1 and k_g^2 were 2.682×10^{-3} and 2.544 along the crystal's length, 6.072×10^{-4} and 2.520 along

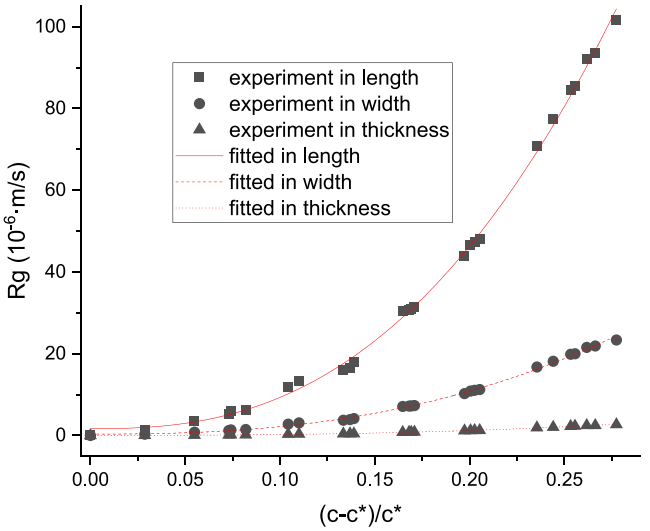

Figure 12. Growth rates of the PX crystal in each of the three dimensions.

its width, and 7.282×10^{-5} and 2.560 in the thickness direction, and the standard relative deviations were 0.103 or lower.

$$R_g(T, c) = k_g^1\left(\frac{c - c^*}{c^*}\right)^{k_g^2} \tag{14}$$

2.4. Heat Transfer. In the crystallizer (see Figure 1), a low temperature was maintained by the coolant outside the crystallizer wall as detailed in Figure 13, where the inner

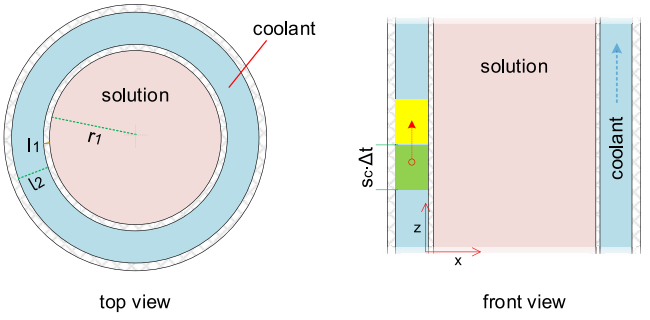

Figure 13. Structure of the jacket scraping-cooling crystallizer.

radius, thickness of wall, width of jacket, and crystallizer height are r_1, l_1, l_2, and h_1, respectively. The coolant moved upward at a flow rate of f_c, at inlet temperature T_c^0, and removed heat from solution in doing so, thereby causing the temperature $T_c(t, z)$ to increase along the z direction. The solution was assumed to be mixed well within the crystallizer and had a uniform temperature $T_s(t)$. The cross-sectional area A_c and flow velocity s_c of the coolant can be calculated by eqs 15 and 16. Assuming a time step Δt, the distance moved by the coolant was $s_c\Delta t$. For the section with distance $s_c\Delta t$ (see the green section in Figure 13), the heat exchange area can be written as $2\pi s_c\Delta t(r_1 + l_1)$ and the corresponding heat flux $q(t, z)$ and heat flow $Q(t, z, s_c\Delta t)$ can be obtained using eqs 17 and 18, respectively. The transfer of heat reduced the temperature

https://doi.org/10.1021/acsomega.3c00069
ACS Omega 2023, 8, 12899−12910

$T_s(t)$ within the crystallizer and increased the temperature $T_c(t, z)$ of the coolant as per eqs 19 and 20, respectively.

$$A_c = \pi(r_1 + l_1 + l_2)^2 - \pi(r_1 + l_1)^2 \tag{15}$$

$$s_c = \frac{f_c}{A_c} \tag{16}$$

$$q(t, z) = -k\frac{T_s(t) - T_c(t, z)}{l_1} \tag{17}$$

$$Q(t, z, s_c\Delta t) = 2\pi s_c \Delta t(r_1 + l_1)q(t, z) \tag{18}$$

$$T_c(t + \Delta t, z + s_c\Delta t) = T_c(t, z) + \frac{Q(t, z, s_c\Delta t)}{s_c\Delta t A_c C_p^c} \tag{19}$$

$$T_s(t + \Delta t) = T_s(t) - \frac{\int Q(t, z, s_c\Delta t)\mathrm{d}z + Q_m}{\pi(r_1^2h_1 + r_2^2h_2)C_p^s} \tag{20}$$

where k is heat conductivity; C_p^c and C_p^s are the heat capacity of the coolant and solution, respectively; Q_m is the heat change caused by crystal nucleation and growth; and r_2 and h_2 are the inner radius and height of the growth vessel in Figure 1, respectively. In consideration of the continuous feed f_s with temperature T_s^0 introduced into the growth vessel, eq 20 can be re-written as

$$T_s'(t + \Delta t) = \frac{T_s(t + \Delta t)C_p^s[\pi(r_1^2h_1 + r_2^2h_2) - f_s] + T_s^0 f_s C_p^s}{\pi(r_1^2h_1 + r_2^2h_2)C_p^s} \tag{21}$$

The above equations were solved using the discretization approach, which discretized the operating time and the crystallizer's function into smaller units. The algorithm was implemented in MATLAB, where the initial temperatures of the crystallizer and coolant along the z direction were assumed to be T_s^0 and T_c^0, and the calculation was iterated with time until the temperature within the crystallizer was stable.

3. PROCESS OPTIMIZATION MODELS

3.1. Multidimensional Population Balance Equation.

The distribution of the crystals' size can be reliably described by the number population density function $\psi(L_1, L_2, L_3, t)$, where L_1, L_2, and L_3 represent the width, length, and thickness of the crystal, respectively, and t is time. The number population density change is written as follows:[24]

$$\frac{1}{V_c(t)}\frac{\partial[\psi(L_1, L_2, L_3, t)V_c(t)]}{\partial t} + \frac{\partial[R_g(T, c, L_1)\psi(L_1, L_2, L_3, t)]}{\partial L_1} + \frac{\partial[R_g(T, c, L_2)\psi(L_1, L_2, L_3, t)]}{\partial L_2} + \frac{\partial[R_g(T, c, L_3)\psi(L_1, L_2, L_3, t)]}{\partial L_3} + \frac{f_s\psi(L_1, L_2, L_3, t)}{V_c(t)} = R_n^c(t) + R_a^c(t) - R_b^c(t) \tag{22}$$

where $V_c(t)$ is the volume of the crystallizer and growth vessel (which was $\pi(r_1^2h_1 + r_2^2h_2)$ in this work), f_s is the inlet and outlet flow rate, $R_g(T, c, L)$ is the growth rate of the crystal in the L direction, $R_n^c(t)$ is the total nucleation rate, and $R_a^c(t)$ and $R_b^c(t)$ are the aggregation and breakage rates, respectively. However, aggregation and breakage were not considered due to being of second importance. Equation 22 can then be simplified to yield the following expression:

$$\frac{\partial\psi(L_1, L_2, L_3, t)}{\partial t} + \frac{\partial[R_g(T, c, L_1)\psi(L_1, L_2, L_3, t)]}{\partial L_1} + \frac{\partial[R_g(T, c, L_2)\psi(L_1, L_2, L_3, t)]}{\partial L_2} + \frac{\partial[R_g(T, c, L_3)\psi(L_1, L_2, L_3, t)]}{\partial L_3} + \frac{f_s\psi(L_1, L_2, L_3, t)}{\pi(r_1^2h_1 + r_2^2h_2)} = R_n^c(t) \tag{23}$$

To solve the population balance equation, the population number function $N(L_1^i, L_2^j, L_3^k, t)$ was defined using eq 24 to represent the number of particles within the range $L_1^{i-1} \le L_1 \le L_1^i$, $L_2^{j-1} \le L_2 \le L_2^j$, and $L_3^{k-1} \le L_3 \le L_3^k$, which was defined as cell $C(i, j, k, t)$, where L_1, L_2, and L_3 were discretized into consecutive segments, with i, j, and k representing the appropriate segment indexes, respectively.

$$N(L_1^i, L_2^j, L_3^k, t) = \int_{L_1^{i-1}}^{L_1^i}\int_{L_2^{j-1}}^{L_2^j}\int_{L_3^{k-1}}^{L_3^k}\psi(L_1, L_2, L_3, t)\,\mathrm{d}L_1\mathrm{d}L_2\mathrm{d}L_3 \tag{24}$$

Particles enter and leave cell $C(i, j, k, t)$ in three directions (width, length, and thickness) caused by nucleation and growth. The quantified accumulation $N^c(L_1^i, L_2^j, L_3^k, t)$ along the width direction can be defined as:

$$N_1^c(L_1^i, L_2^j, L_3^k, t) = R_g(T, c, L_1)\Delta t\{[a_{i-1}N(L_1^{i-1}, L_2^j, L_3^k, t) + b_{i-1}N(L_1^i, L_2^j, L_3^k, t)] - [a_iN(L_1^i, L_2^j, L_3^k, t) + b_iN(L_1^{i+1}, L_2^j, L_3^k, t)]\} \tag{25}$$

in which

$$a_i = \frac{\Delta C_1^{i+1}}{\Delta C_1^i(\Delta C_1^{i+1} + \Delta C_1^i)} \tag{26}$$

$$b_i = \frac{\Delta C_1^i}{\Delta C_1^{i+1}(\Delta C_1^{i+1} + \Delta C_1^i)} \tag{27}$$

where ΔC_1^i is the size interval of cell $C(i, j, k, t)$ in the width direction and Δt is the time interval. The accumulation along the length and thickness directions follows the same principle, as shown in eqs 25−27, from which the updated population number can be derived:

https://doi.org/10.1021/acsomega.3c00069
ACS Omega 2023, 8, 12899−12910

$$N(L_1^i, L_2^j, L_3^k, t + \Delta t) = N(L_1^i, L_2^j, L_3^k, t) + \sum_{m=1}^{3} N_m^c(L_1^i, L_2^j, L_3^k, t) \quad (28)$$

At each time step, the number of particles in each cell $C(i, j, k, t)$ and the solution concentration were updated, and using the assembled crystallization kinetic models allowed calculation of the nucleation and growth rates.

3.2. Equation-Oriented Modeling for Process Solving. For a general multi-phase unit in crystallization separation process, the mass and energy balance structures have following forms:[25]

$$f_M(T, x, f^L, f^S) = M_{i,\text{in}}^L + M_{i,\text{in}}^S - M_{i,\text{out}}^L - M_{i,\text{out}}^S = 0 \quad (29)$$

$$f_H(T, x, f^L, f^S) = H_{\text{in}}^L + H_{\text{in}}^S - H_{\text{out}}^L - H_{\text{out}}^S + Q_{\text{ext}} + Q_{\text{gen}} = 0 \quad (30)$$

where the superscripts L and S represent liquid and solid phases, respectively. f_M and f_H are the mass balance and energy balance equations, respectively. T, x, f^L, and f^S are the temperature, composition, liquid flow, and solid flow of the stream. M_i is the molar flow for each compound i, H is the energy flow rate, Q_{ext} is the external heat removed from mixture, and Q_{gen} is the energy generated by crystallization process. The molar flow M_i can be calculated by the mother liquor molar fraction x_i, molar flow f^L, and the particle number distribution $N_i(L_1, L_2, L_3, t)$:

$$M_i = f^L x_i + \iiint_{L_3} (L_1 L_2 L_3) \rho N_i(L_1, L_2, L_3, t)\, \mathrm{d}L_1 \mathrm{d}L_2 \mathrm{d} \quad (31)$$

where ρ is the molar density of crystal. The energy flow rate H can be calculated by classical thermodynamic models. The generated energy Q_{gen} is mainly caused by the crystallization of crystals, which can be calculated by

$$Q_{\text{gen}} = \iiint [N_{\text{out}}(L_1, L_2, L_3, t) - N_{\text{in}}(L_1, L_2, L_3, t)] (L_1 L_2 L_3) \Delta H_m \rho \mathrm{d}L_1 \mathrm{d}L_2 \mathrm{d}L_3 \quad (32)$$

where ΔH_m is the molar melting enthalpy.

For the units in the process presented in Figure 1, all the mass balance and energy balance equations can be given as

$$\begin{bmatrix} f_{M,1}(T, x, f^L, f^S) \\ f_{H,1}(T, x, f^L, f^S) \\ f_{M,2}(T, x, f^L, f^S) \\ f_{H,2}(T, x, f^L, f^S) \\ f_{M,3}(T, x, f^L, f^S) \\ f_{H,3}(T, x, f^L, f^S) \end{bmatrix} = \begin{bmatrix} R_{M,1} \\ R_{H,1} \\ R_{M,2} \\ R_{H,2} \\ R_{M,3} \\ R_{H,3} \end{bmatrix} \approx \mathbf{0} \quad (33)$$

where 1,2, and 3 represent the crystallizer, growth vessel, and wash column, respectively. R_M and R_H are the residual values corresponding to the convergence error of equations. The independent variables are the temperature T, liquid phase composition x, liquid flow f^L, and solid flow f^S within each unit and stream; assuming $\boldsymbol{\tau} = [T \quad x \quad f^L \quad f^S]$, eq 33 can be transformed into a Jacobian matrix:

$$\boldsymbol{J} = \begin{bmatrix} \frac{\partial f_{M,1}}{\partial \tau_1} & \cdots & \frac{\partial f_{M,1}}{\partial \tau_n} \\ \vdots & \ddots & \vdots \\ \frac{\partial f_{M,3}}{\partial \tau_1} & \cdots & \frac{\partial f_{M,3}}{\partial \tau_n} \end{bmatrix} \quad (34)$$

The equations were solved in MATLAB, different with the ordinary equation-oriented equations. The particle number distribution $N(L_1, L_2, L_3, t)$ is a function of time t; therefore, the solution program was implemented with a time step of 1 s; the equation-oriented equations converged at each time point. Calculations were stopped after the temperature and particle number distribution were stable.

3.3. Models for Process Optimization. For a given actual existing process as presented in Figure 1, the control variables for optimizing the crystallization separation are feed flowrate f_s (with inlet temperature T_s^0), coolant flowrate f_c (with inlet temperature T_c^0), and feed concentration c^0. Together, they are defined as $\boldsymbol{\vartheta}$[26]

$$\boldsymbol{\vartheta} = [f_s \quad T_s^0 \quad f_c \quad T_c^0 \quad c^0]^T \quad (35)$$

Meanwhile, the target variables are the final product purity c^P, product yield ξ, and energy cost κ. Some constraints should be considered for the variables in $\boldsymbol{\vartheta}$, especially the reduced limits for the following:

(1) the PX product purity c^P, which is a product specification. As a function of crystal size distribution and wash intensity during the centrifuging phase, the impurity is mainly caused by the mother liquor;
(2) the coolant temperature T_c^0, which is restricted by the refrigerator capacity and the freezing medium's properties. Additionally, the crystal's morphology is affected by supersaturation (see Figure 3), which is itself a function of the mother liquor temperature. Therefore, T_c^0 should be controlled to obtain the desired particles; and
(3) the PX product yield ξ (a function of particle size distribution), because smaller particles may pass through the filter or melt during centrifuge and wash.

The optimal operating conditions maximize product purity c^P and yield ξ, as well as minimize energy cost κ by adjusting the control variables in $\boldsymbol{\vartheta}$. However, achieving the ideal values for c^P, ξ, and κ at the same time is a pseudo-proposition. Traditionally, a lower limit is given for product purity c_{min}^P, after which the process operating conditions are adjusted to achieve an optimal economic benefit ϕ:

$$\phi = f_s \xi \chi^P - f_c \kappa \chi^c \quad (36)$$

where χ^P and χ^c are the costs of the PX product and coolant energy, respectively.

4. RESULTS AND DISCUSSION

4.1. Model Validation. We carried out an investigation on the process presented in Figure 1; the feed mass compositions

https://doi.org/10.1021/acsomega.3c00069
ACS Omega 2023, 8, 12899−12910

of PX, OX, MX, and EB were 0.84, 0.04, 0.10, and 0.02, respectively. The feed mass flow was 0.8 kg/s. The inner diameter and height of the crystallizer and growth vessel were 0.4 and 1 m, respectively. The high-purity ethyl alcohol was used as coolant, the flowrate and temperature of coolant were 15 kg/s and 250 K, respectively, and the heat capacity C_p^c was assumed to be 2.1 kJ/(kg·K).[27] The crystallizer wall was steel, and thus, its heat conductivity k was 45 W/(mK). The coolant was treated as cooled by electricity, with a price of power of approximately \$5.302 × 10^{-5}/kJ (in China), and electrical efficiency of 60%. The heat capacity C_p^s of the solution was calculated as the average of the xylenes' heat capacities, and the average value was found to be 1.65 kJ/(kg·K).[28] The fusion enthalpy of PX is approximately 159.50 kJ/kg, the domestic selling price of PX was assumed to be \$1.263/kg, and only the particles with length equal to or longer than 2 mm were assumed to be retained in the wash column, presumably yielding a high-purity product.

The simulated process became stable after 20 min, and the change of particle size distribution of final product is presented in Figure 14, which indicates that the shape of particles is

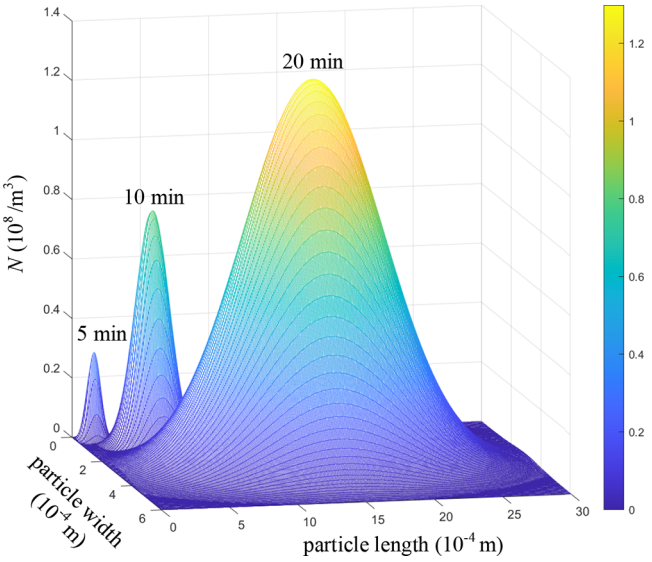

Figure 14. Predicted particle number distribution with size at different time points.

uniformly distributed and the uniform distribution will reduce the loss and enhance the yield during the washing, sweeting, and centrifuge procedures.

Experiments were also carried out on the same process proposed in simulation; the particle number distributions with crystal width and length of the final product, $N_{e,w}$ and $N_{e,l}$, were detected by the morphology approach and compared with the predicted results $N_{s,w}$ and $N_{s,l}$ in Figure 15. The average relative deviation between $N_{e,w}$ and $N_{s,w}$ and between $N_{e,l}$ and $N_{s,l}$ was found to be 3.5%, which confirms the accuracy of proposed models.

4.2. Process Optimization. The optimization methodology proposed in previous sections was applied to the same process, which kept the feed conditions and equipment parameters constant, and just adjusted the flowrate and inlet temperature of the coolant. The optimization algorithm was performed in MATLAB after the operating conditions became steady. The distribution of the economic benefit ϕ with

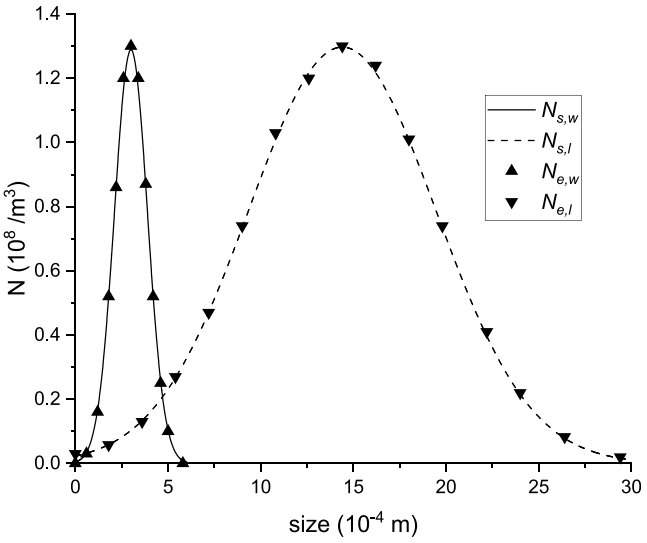

Figure 15. Comparison of particle number distribution between experiment and simulation, $N_{e,w}$ and $N_{e,l}$ are the measured particle number distribution with width and length, respectively; $N_{s,w}$ and $N_{s,l}$ are the corresponding simulated results.

coolant flowrate f_c and inlet temperature T_c^0 is shown in Figure 16, which indicates that the temperature and flowrate of

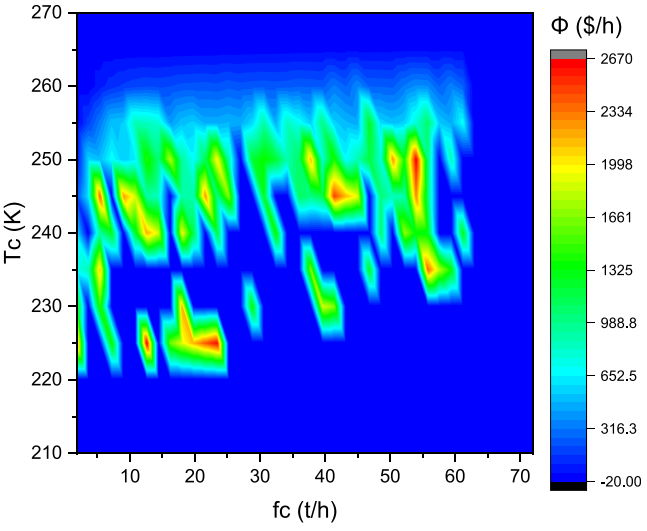

Figure 16. Economic benefit ϕ distribution with coolant flowrate f_c and inlet temperature T_c^0.

coolant should be well arranged to achieve the best economic benefit. The economic effect becomes desultory when the coolant flowrate is increased further and/or the coolant temperature is reduced further beyond these ranges, because OX will also precipitate at lower temperatures, meaning that the PX product will not meet the standard requirements.

The effect of residence time, which is manipulated by feed flowrate, was also investigated. By keeping the operating conditions of coolant, equipment, and feed composition similar with that in Section 4.1, the economic benefit ϕ distribution with feed flowrate f_s is given in Figure 17, which indicates that the feed flowrate has an optimal value.

https://doi.org/10.1021/acsomega.3c00069
ACS Omega 2023, 8, 12899−12910

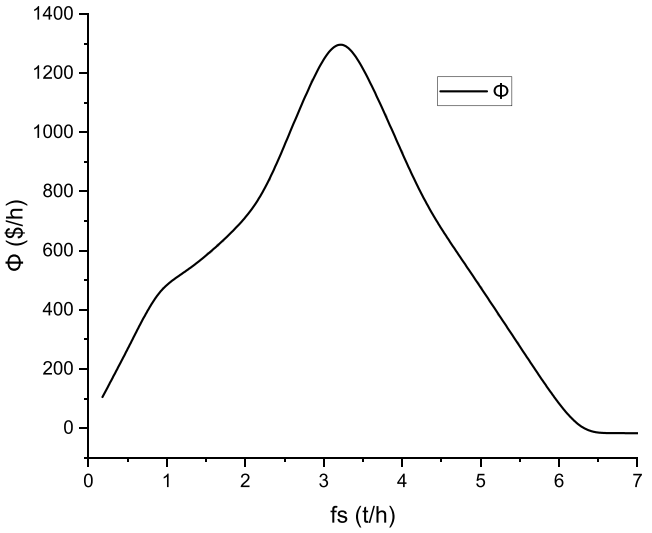

Figure 17. Economic benefit ϕ distribution with feed flowrate f_s

5. CONCLUSIONS

In previously published works investigating the problem described here, crystal size was most often measured by slurry transmittance or shadow area and then represented by a sphere (i.e., with uniform dimensions). Few studies used more than one camera, which is not considered an appropriate method for deep cold conditions. For this investigation, a novel monocular 3D reconstruction technique was proposed as a means to measure a crystal's discrete dimensions (i.e., length, width, and thickness), from which the growth kinetics of the PX crystal can be derived. Nucleation kinetics of the PX crystals as they formed on the inner wall of the crystallizer unit and in solution were also measured, and the trends were predicted. Since PX's nucleation and growth kinetics are both functions of supersaturation, an activity coefficient-based model was adopted to predict solubility of organic mixtures, and the binary parameters of xylene mixtures were correlated from experimental data.

A multi-dimensional population balance equation and its solving algorithm were developed and presented, and applied to a real PX crystallization separation process. The coolant moved along the jacket of the crystallizer and withdrew heat from the solution, necessitating equations to predict the temperatures of these two systems, which then allowed derivation of the rate of nucleation. The proposed models were implemented in MATLAB and simulated on a process with specific device parameters and feed conditions. From this, the distribution of economic benefit, with respect to the temperature and flowrate of coolant, as well as the feed flowrate, was investigated, ultimately revealing the optimal operating conditions.

ASSOCIATED CONTENT

Supporting Information

The Supporting Information is available free of charge at https://pubs.acs.org/doi/10.1021/acsomega.3c00069.

(PDF)

AUTHOR INFORMATION

Corresponding Author

Chaohe Yang − *State Key Laboratory of Heavy Oil Processing, China University of Petroleum Huadong, Qingdao 266580, China;* orcid.org/0000-0001-6995-9170; Email: yangch@upc.edu.cn

Authors

Zhenxing Cai − *State Key Laboratory of Heavy Oil Processing, China University of Petroleum Huadong, Qingdao 266580, China;* orcid.org/0000-0003-0572-406X

Hui Zhao − *State Key Laboratory of Heavy Oil Processing, China University of Petroleum Huadong, Qingdao 266580, China;* orcid.org/0000-0002-5076-6325

Pingxin Li − *State Key Laboratory of Heavy Oil Processing, China University of Petroleum Huadong, Qingdao 266580, China*

Xiaobo Chen − *State Key Laboratory of Heavy Oil Processing, China University of Petroleum Huadong, Qingdao 266580, China;* orcid.org/0000-0001-9180-0190

Complete contact information is available at: https://pubs.acs.org/10.1021/acsomega.3c00069

Notes

The authors declare no competing financial interest.

ACKNOWLEDGMENTS

This work was supported by the National Natural Science Foundation of China (22078364).

NOMENCLATURE

symbol definition
A_c cross-sectional area, m^2
b_{ij} binary parameters of the UNIQUAC model
c and c^* concentration and saturated concentration
c^P product purity
f_c flow rate of coolant, kg/s
f_s flow rate of feed, kg/s
f_M mass balance equation
f_H energy balance equation
ΔH_m molar melting enthalpy, J/mol
k_n^1 and k_n^2 parameters for nucleation rate
q heat flux, W/m^2
Q heat flow, W
N population number function
R universal gas constant
r_1, l_1, l_2, and h_1 inner radius, thickness of wall, width of jacket, and height of crystallizer, m
r_2 and h_2 inner radius and height of growth vessel, m
R_n nucleation rate, $m^{-3}s^{-1}$
R_g growth rate, m/s
s_c flow velocity of coolant, m/s
T temperature, K
T_m normal melting point, K
T_c^0 inlet temperature of coolant, K
T_s temperature of solution, K
Δt time step, s
x_i concentration of compound i
χ^P prices of PX product, $/kg
χ^c prices of coolant energy, $/J
ϕ economic benefit
γ_i activity coefficient

https://doi.org/10.1021/acsomega.3c00069
ACS Omega 2023, 8, 12899−12910

ψ number population density function
ρ molar density of crystal, mol/m^3
κ energy cost
ξ product yield

REFERENCES

(1) Patience, D. B.; Rawlings, J. B.; Mohameed, H. A. Crystallization of para-xylene in scraped-surface crystallizers. *AIChE J.* **2001**, *47*, 2441−2451.
(2) Zhang, J.; Zhu, X.; Zhang, S.; Cheng, M.; Yu, M.; Wang, G.; Li, C. Selective production of para-xylene and light olefins from methanol over the mesostructured Zn−Mg−P/ZSM-5 catalyst. *Catal. Sci. Technol.* **2019**, *9*, 316−326.
(3) Allan, S.; Myerson, D. E.; Alfred Y., Lee *Handbook of Industrial Crystallization 3rd Edition*; Cambridge University Press, 2019.
(4) Jakob, A.; Joh, R.; Rose, C.; Gmehling, J. Solid-liquid equilibria in binary mixtures of organic compounds. *Fluid Phase Equilib.* **1995**, *113*, 117−126.
(5) De Goede, R.; Van Rosmalen, G.; Hakvoort, G. Solid-liquid equilibria in para−/meta-xvlene and para−/ortho-xylene binary mixtures at atmospheric pressure. *Thermochim. Acta* **1989**, *156*, 299−312.
(6) De Goede, R.; Van Rosmalen, G. Crystal growth phenomena of paraxylene crystals. *J. Cryst. Growth* **1990**, *104*, 399−410.
(7) Mohameed, H.; Jdayil, B. A.; Takrouri, K. Separation of para-xylene from xylene mixture via crystallization. *Chem. Eng. Process.: Process Intesif.* **2007**, *46*, 25−36.
(8) Costa Reis, M. Current Trends in Predictive Methods and Electrolyte Equations of State. *ACS Omega* **2022**, 16847.
(9) Alshehri, S.; Hussain, A.; Ahsan, M. N.; Ali, R.; Siddique, M. U. M. Thermodynamic, computational solubility parameters in organic solvents and in silico GastroPlus based prediction of ketoconazole. *ACS Omega* **2021**, *6*, 5033−5045.
(10) Buchowski, H.; Ksiazczak, A.; Pietrzyk, S. Solvent activity along a saturation line and solubility of hydrogen-bonding solids. *J. Phys. Chem.* **1980**, *84*, 975−979.
(11) Yerkenov, T.; Tazikeh, S.; Tatar, A.; Shafiei, A. Asphaltene Precipitation Prediction during Bitumen Recovery: Experimental Approach versus Population Balance and Connectionist Models. *ACS Omega* **2022**, *7*, 33123−33137.
(12) Cai, Z.; Zhao, H.; Zhou, X.; Chen, X.; Yang, C. Determination and modeling of binary solid-liquid equilibria of para-xylene/meta-xylene, para-xylene/ortho-xylene by DSC method. *Fluid Phase Equilib.* **2022**, *554*, 113325.
(13) Gmehling, J. G.; Anderson, T. F.; Prausnitz, J. M. Solid-liquid equilibria using UNIFAC. *Ind. Eng. Chem. Fundam.* **1978**, *17*, 269−273.
(14) Boudouh, I.; Tamura, K.; Djemai, I.; Robustillo-Fuentes, M. D.; Hadj-Kali, M. K. Solid−Liquid Equilibria for Biphenyl+ n-Tetracosane Binary Mixtures and n-Tetracosane+ Dibenzofuran+ Biphenyl Ternary Mixtures: Experimental Data and Prediction with UNIFAC Models. *Int. J. Thermophys.* **2022**, *43*, 1−18.
(15) Valavi, M.; Svard, M.; Rasmuson, Å. C. Prediction of the solubility of medium-sized pharmaceutical compounds using a temperature-dependent NRTL-SAC model. *Ind. Eng. Chem. Res.* **2016**, *55*, 11150−11159.
(16) Ely, D. R.; García, R. E.; Thommes, M. Ostwald−Freundlich diffusion-limited dissolution kinetics of nanoparticles. *Powder Technol.* **2014**, *257*, 120−123.
(17) Venables, J. Rate equation approaches to thin film nucleation kinetics. *Philos. Mag.* **1973**, *27*, 697−738.
(18) Xie, R.; Li, Z.; Peng, X. Nucleation kinetics vs chemical kinetics in the initial formation of semiconductor nanocrystals. *J. Am. Chem. Soc.* **2009**, *131*, 15457−15466.
(19) Videla, A. R.; Polanco, C.; Escalona, N. Phenomenological model of the effect of organic polymer addition on the control of ammonium nitrate caking. *Powder Technol.* **2017**, *315*, 114−125.
(20) Hounslow, M.; Lewis, A.; Sanders, S.; Bondy, R. Generic crystallizer model: I. A model framework for a well-mixed compartment. *AIChE J.* **2005**, *51*, 2942−2955.
(21) Wang, X. Z.; Roberts, K. J.; Ma, C. Crystal growth measurement using 2D and 3D imaging and the perspectives for shape control. *Chem. Eng. Sci.* **2008**, *63*, 1173−1184.
(22) Liu, Y.; Tan, J.; Wan, M.; Zhang, L.; Yao, X. Quantitative measurement of OH* and CH* chemiluminescence in jet diffusion flames. *ACS Omega* **2020**, *5*, 15922−15930.
(23) Liao, C.; Tarng, Y. On-line automatic optical inspection system for coarse particle size distribution. *Powder Technol.* **2009**, *189*, 508−513.
(24) Puel, F.; Févotte, G.; Klein, J. Simulation and analysis of industrial crystallization processes through multidimensional population balance equations. Part 1: a resolution algorithm based on the method of classes. *Chem. Eng. Sci.* **2003**, *58*, 3715−3727.
(25) Ambrosy, J. M.; Pasel, C.; Luckas, M.; Bittig, M.; Bathen, D. Influence of oxygen on Hg0 adsorption on non-impregnated activated carbons. *ACS Omega* **2020**, *5*, 17051−17061.
(26) Seki, H.; Amano, S.; Emoto, G. Modeling and control system design of an industrial crystallizer train for para-xylene recovery. *J. Process Control* **2010**, *20*, 999−1008.
(27) Kelley, K. K. The Heat Capacities of Ethyl and Hexyl Alcohols from 16 K. to 298 K. and the Corresponding Entropies and Free Energies. *J. Am. Chem. Soc.* **1929**, *51*, 779−786.
(28) Prrznn, K. S.; Scori, D. W. *The Thermodynamics and Molecular Structure of Benzene and Its Methyl Derivatives.*

https://doi.org/10.1021/acsomega.3c00069
ACS Omega 2023, 8, 12899−12910